

Model improvements to simulate charging in SEM

Arat, K. T.; Klimpel, T.; Hagen, C. W.

DOI

[10.1117/12.2297478](https://doi.org/10.1117/12.2297478)

Publication date

2018

Document Version

Final published version

Published in

Metrology, Inspection, and Process Control for Microlithography XXXII

Citation (APA)

Arat, K. T., Klimpel, T., & Hagen, C. W. (2018). Model improvements to simulate charging in SEM. In V. A. Ukraintsev, & O. Adan (Eds.), *Metrology, Inspection, and Process Control for Microlithography XXXII* (Vol. 10585). Article 1058518 SPIE. <https://doi.org/10.1117/12.2297478>

Important note

To cite this publication, please use the final published version (if applicable). Please check the document version above.

Copyright

Other than for strictly personal use, it is not permitted to download, forward or distribute the text or part of it, without the consent of the author(s) and/or copyright holder(s), unless the work is under an open content license such as Creative Commons.

Takedown policy

Please contact us and provide details if you believe this document breaches copyrights. We will remove access to the work immediately and investigate your claim.

Green Open Access added to TU Delft Institutional Repository

'You share, we take care!' - Taverne project

<https://www.openaccess.nl/en/you-share-we-take-care>

Otherwise as indicated in the copyright section: the publisher is the copyright holder of this work and the author uses the Dutch legislation to make this work public.

PROCEEDINGS OF SPIE

SPIDigitalLibrary.org/conference-proceedings-of-spie

Model improvements to simulate charging in SEM

Arat, K., Klimpel, T., Hagen, C.

K. T. Arat, T. Klimpel, C. W. Hagen, "Model improvements to simulate charging in SEM," Proc. SPIE 10585, Metrology, Inspection, and Process Control for Microlithography XXXII, 1058518 (13 March 2018); doi: 10.1117/12.2297478

SPIE.

Event: SPIE Advanced Lithography, 2018, San Jose, California, United States

Model improvements to simulate charging in SEM

K. T. Arat^{*a}, T. Klimpel^b, C. W. Hagen^a

^aFaculty of Applied Sciences, Delft University of Technology, Lorentzweg 1, 2628CJ Delft, The Netherlands;

^bGenISys GmbH, Eschenstrasse 66, Taufkirchen (Munich), D-82024, Germany.

ABSTRACT

Charging of insulators is a complex phenomenon to simulate since the accuracy of the simulations is very sensitive to the interaction of electrons with matter and electric fields. In this study, we report model improvements for a previously developed Monte-Carlo simulator to more accurately simulate samples that charge. The improvements include both modelling of low energy electron scattering and charging of insulators. The new first-principle scattering models provide a more realistic charge distribution cloud in the material, and a better match between non-charging simulations and experimental results. Improvements on charging models mainly focus on redistribution of the charge carriers in the material with an induced conductivity (EBIC) and a breakdown model, leading to a smoother distribution of the charges. Combined with a more accurate tracing of low energy electrons in the electric field, we managed to reproduce the dynamically changing charging contrast due to an induced positive surface potential.

Keywords: Charging, SEM, Monte-Carlo simulation, EBIC, Breakdown, Low Energy Electrons

1. INTRODUCTION

Electron beam-based inspection techniques have become a standard where nanometer resolution imaging is required for state of the art semiconductor devices. However, when non-conductive materials are involved, charging occurs and issues are reported such as image distortions due to the primary beam deflections [1]–[5] and image contrast changes due to the changing secondary electron (SE) emission [6], [7, p. 127], [8]. As a consequence measurements of critical dimensions (CD) will be less accurate [9]–[11]. Therefore, a better understanding of the charging effects on electron imaging becomes crucial for metrology.

Several Monte-Carlo studies were reported that included charging effects, but they rather focused on simulations for simplified geometries such as semi-infinite surfaces [12]–[14]. Besides that, some Monte-Carlo simulators were developed to simulate full 3D geometries and charging models were also incorporated [15]–[19]. However, the long calculation times of these simulators renders them quite impractical for realistic scenarios.

In an earlier paper, we reported a Monte-Carlo simulator, that included charging effects, making use of a multigrid-based electric field solver to decrease the electric field computation time [20]. Combining the electric field solver with a semi-empirical electron-matter interaction model, we were able to simulate an SEM image of an area of $\sim 1.5 \mu\text{m}^2$ of grating couplers, shown in Figure 1a, in about 1 hour [20]. However, the shadowing phenomenon (bright-to-dark transition) on the oxide pads, seen in Figure 1a, could not be reproduced in the simulation (Figure 1c). Including the charging model only led to a blur of the edges due to beam deflection, see Figure 1b and c.

To properly include the charging effects, it is important to accurately model the electron-matter interaction, especially low energetic electrons which are very sensitive to the local electric fields. Therefore, improvements are needed of both the electron scattering models and the charging models. In this work, we report our attempts to improve both.

First, we improved the electron scattering models by incorporating discrete scattering of electrons instead of the continuous slowing down approximation (CSDA). Inelastic scattering is modeled using the dielectric function. Electron-phonon scattering and quantum mechanical transmission through boundaries is implemented. Moreover, solid-state effects on the atomic potential are taken into account in modelling the elastic scattering. All electrons are traced until their energy is below the surface barrier of approximately 10 eV.

*k.t.arat@tudelft.nl

Experiment

Simulations

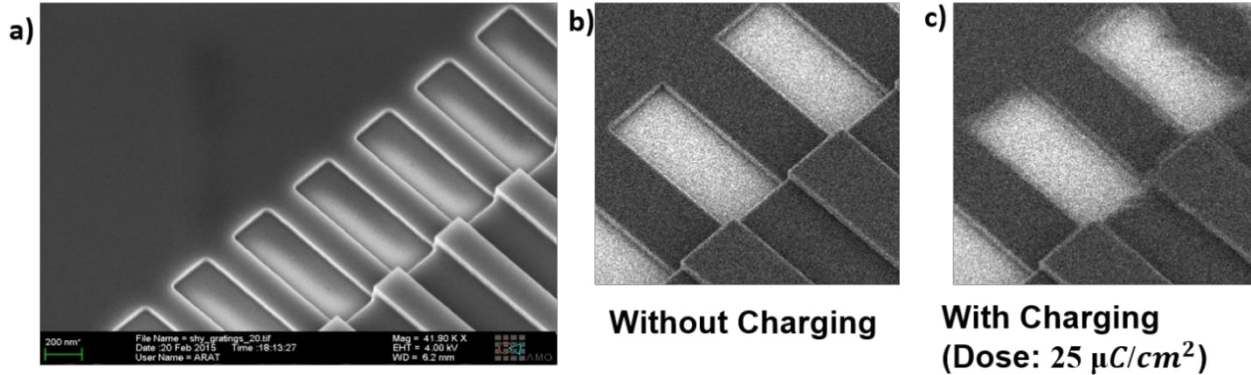


Figure 1 – a) Grating coupler experimental SEM image [20] compared with b) the simulated image without charging, and c) the simulated image with charging taken into account.

Secondly, we addressed issues exclusive to insulators, namely charge redistribution to include effects such as e-beam induced conductivity (EBIC). The simplest approach would be to completely ignore charge redistribution in insulators, as was done in our previous study [20], or only consider catastrophic effects like dielectric breakdown. The other extreme would be modeling from first principles including effects like electron-hole recombination and trapping. We chose a midway and modeled the charge redistribution effects using phenomenological models with a limited number of calibration parameters [21].

After that, the effect of charging on the electron emission from a bulk oxide sample during a linescan, for different doses, is demonstrated. Subsequently, a top-down view of the grating couplers is simulated where the charging (bright-to-dark) contrast is present. Finally, the impact of the charge redistribution model is shown on a test sample with four metal contact pads embedded in a thin SiO₂ layer on top of a Si wafer. Three pads are electrically floating (no contact to the underlying Si wafer), and the fourth one is connected to the underlying Si wafer. The effect on the simulated SEM images is shown when the charging and/or EBIC model is switched on. The new models clearly lead to more realistic images and can reproduce phenomena that were not possible to reproduce with the previous models.

2. SCATTERING MODEL

We will now first describe the scattering model improvements, and assume that the scattering cross-sections do not change due to charging. The electron trajectories are influenced by the charge clouds in the materials, which are formed by electrons getting trapped (negative charge) or electrons generating new electrons (both negative and positive charge). Hence, accurate modelling of electron generating, transport and boundary crossing is important to understand the charge distribution in the material and the electron emission.

In our previous study [20], the semi-empirical scattering models were designed to get an accurate SE yield value for a semi-infinite surface. However, an accurate SE yield does not guarantee a realistic scattering cloud inside the material, as shown in Figure 2a. The deviation from the scattering cloud will not only affect the charging with charge distribution, but also the signal from topographical structures. It is still possible to generate a more realistic scattering cloud with CSDA, such as Figure 2b, by allowing the generation and scattering of the electrons in deeper regions of the material; yet any inaccuracy will lead to a deviation in the charge-up phenomenon. Therefore, we preferred to switch to first principle modelling to determine the charge distribution.

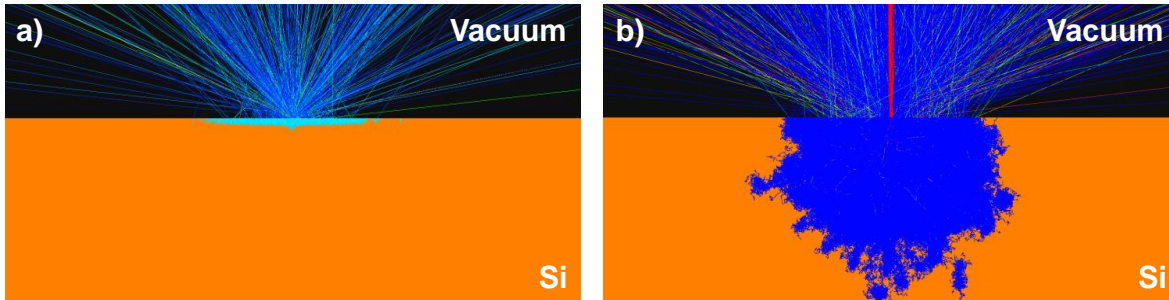


Figure 2 – Scattering cloud of SEs: generic shape of the cloud obtained with a) the approximate (former) models; b) first principle (current) models. In a) only SEs that can escape are generated; b) all SEs are generated and traced.

2.1 Improvements on elastic scattering cross-sections

Previously, Mott cross-sections were used to calculate elastic scattering mean free paths and scattering angles. However, the calculations were calculated for a “free atom” potential which is not appropriate for our applications because it does not include solid state effects. Instead, a “muffin-tin” potential is more realistic. Furthermore, the indistinguishability of the incident electron from the bound electrons, “exchange-correction”, and the polarization of the target atom due to incident electrons, “correlation-polarization”, are also included. All these options are offered by the ELSEPA package [22]. For Si, the “muffin-tin” potential results in ~ 1.5 times larger mean free paths, as seen in Figure 3. At low energies, below a few hundred electron volts (eV), the Mott cross-sections turn out to become very sensitive to the atomic potential [23]. Because at these low energies the quasi-elastic, electron-phonon interaction becomes dominant, we followed the approach suggested by Verduin [24] and use the electron-phonon scattering model for low energies. Therefore, in the present study, the elastic scattering cross-section consists of:

- Mott cross-section (muffin-tin + “exchange correction” + “correlation-polarization”) for energy > 200 eV
- Acoustic phonon scattering cross-section for energy < 100 eV

For energies in between 100 eV and 200 eV, the cross-section is interpolated between the two.

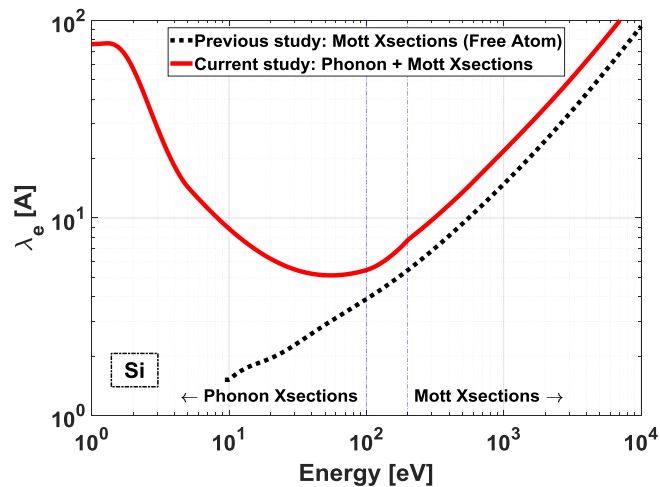


Figure 3 - Elastic mean free path vs. energy for Si: it consists of an interpolation between the Mott cross-section (energy > 200 eV) and phonon cross-sections (energy < 100 eV). The Mott cross-sections were calculated by ELSEPA [22], assuming muffin-tin approximation, exchange correction and correlation-polarization effects.

Material parameters, especially related with acoustic phonons are not easy to find. To serve the interested reader, we list the parameters used in this work in Table 1.

Table 1- Material parameters for Si, Cu and SiO₂

	Si	Cu	SiO₂	
ρ_m [g/cm ³]	2.329 ^[25]	8.96 ^[26]	2.648 ^[27]	
E_F [eV]	7.83	7.0 ^[28]	-	
W or χ [eV]	4.05	4.65 ^[28]	0.9 ^[29]	
E_g [eV]	1.12	-	9.0 ^[29]	
m_{dos} [m_e]	1.08 ^[30]	1.0 ^[24]	1.0 ^[+]	
m_{eff} [m_e]	0.26 ^[30]	1.01 ^[28]	1.0 ^[+]	
A_{ac}	5 ^[+]	5 ^[+]	7 ^[31]	
E_{Ph} [meV]	14 ^[*]	12.6 ^[*]	6.8 ^[*]	
u_s [m/s]	Longitudinal:	9130 ^[32]	4760 ^[28]	3560 ^[31]
	Transversal:	5842 ^[32]	2325 ^[28]	3560 ^[+]
ϵ_{ac} [eV]	Longitudinal:	9.2 ^[33]	4.76 ^[*]	3.4 ^[31]
	Transversal:	5.0 ^[33]	3.72 ^[*]	3.4 ^[+]

Density ρ_m , Fermi energy E_F , work function W , electron affinity χ , band gap E_g at 300° K, density of state mass m_{dos} , effective mass of electron m_{eff} , screening parameter A_{ac} , speed of sound in solid u_s and acoustic deformation potential ϵ_{ac} are given in Table 1. [*] are calculated values and [+] are assumed values. The net-average energy loss in the phonon scattering, E_{Ph} is calculated by the equation 3.116 in Verduin [24].

2.2 Improvements on inelastic scattering cross-sections

In the previous study [20], an algorithm based on CSDA was used to model the energy transfer of the primary electrons (PE) [34]. Although CSDA is a good approximation to estimate stopping power (SP) at high energies, it overestimates the SP at very low energies. Furthermore, it does not describe the SE generation. Therefore, we have employed first principle modelling to simulate the low energetic electrons as accurately as possible. In this study, energy and momentum transfer of an electron to the material is modeled by the dielectric function formalism using optical data [35]. It allows calculation of inelastic events discretely, as depicted in Figure 4.

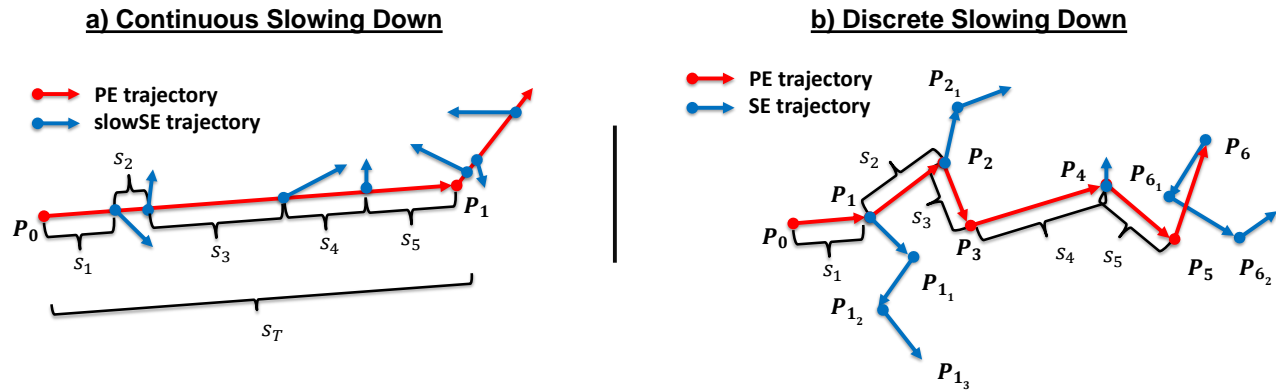


Figure 4 – Inelastic scattering: a) a semi-empirical model is used in the previous study which is based on the CSDA. It estimates the number of (slow) SEs and their energies for a path length (S_T) from the stopping power; b) first principle modeling is used in the current study which is based on dielectric function formalism. It estimates the inelastic mean free path, energy and momentum transfer for each inelastic event (P_1 , P_2 , P_4 , and P_6) based on the energy loss function.

To calculate inelastic cross-sections, we take Ashley's (simple) model [35] and adopted the refinements suggested by Kieft and Bosch [23], i.e. no exchange correction for energies < 50 eV, and restrict energy losses such that electrons cannot end up with an energy lower than the Fermi level. The stopping power from the previous study is compared to the stopping power as obtained from the refined Ashley model in Figure 5b. It is seen to be identical for energies above 1 keV, but deviates at lower energies.

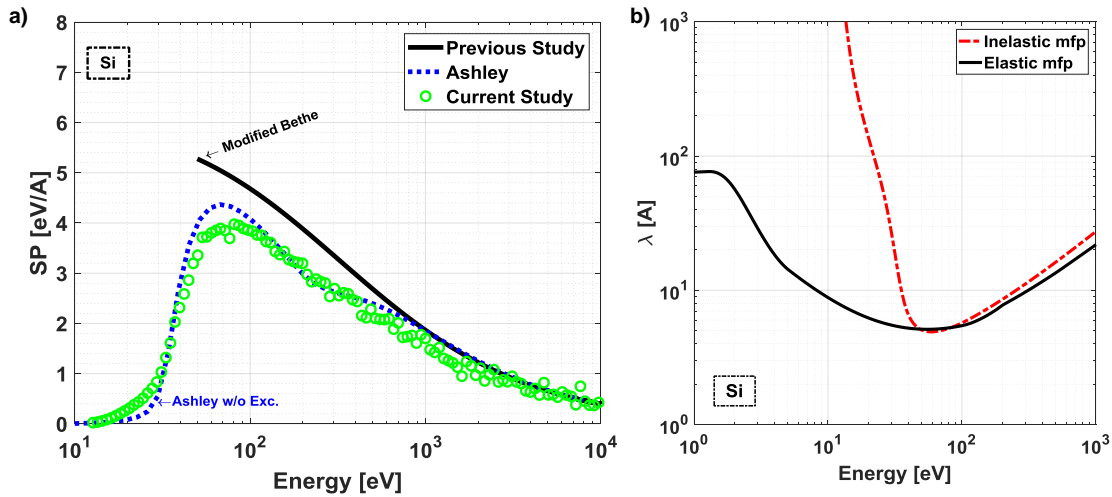


Figure 5 – Modelling inelastic scattering: a) stopping power, b) comparison of mean free paths in the current study.

We obtain the energy transfer using the dielectric function formalism. This, however, does not provide the initial (binding) energy of the secondary electron prior to a scattering event. We model that following the approach suggested by Kieft and Bosch [23].

2.3 Improvements on boundary crossing

The lower the electron energy, the more its path is affected when it interacts with a boundary and as a result it can be reflected or transmitted. Modelling the boundary crossing is crucial for SE emission. In the previous study, the probability to cross the surface barrier was modeled using momentum conservation only. That is, if the electron approaches the surface under an angle bigger than the critical angle (α'_c , see Figure 6), it will be reflected (total internal reflection).

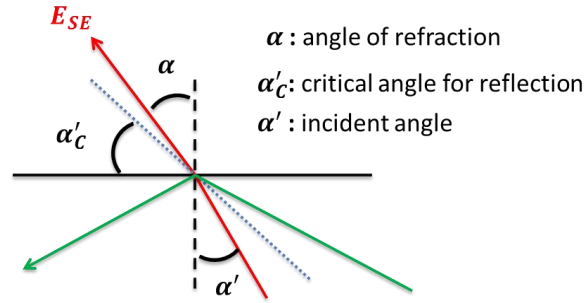


Figure 6 – Transmission of an electron from the surface.

In this study, the probability of transmission is determined quantum mechanically. When the electron is considered as a wave, there is a probability that part of the wave is transmitted through the boundary and part of it is reflected. In the current study we extended the boundary crossing with the quantum mechanical transmission probability [36, p. 17]. Equation 1 gives the probability of transmission for an electron.

$$P(\alpha') = \frac{4 \sqrt{1 + \frac{\Delta U}{E \cos^2 \alpha'}}}{\left(1 + \sqrt{1 + \frac{\Delta U}{E \cos^2 \alpha'}}\right)^2} \quad (1)$$

where ΔU is the change in the kinetic energy; E is electron's kinetic energy and α' is the angle of incidence.

3. CHARGING MODEL

The high-level interaction between the Monte-Carlo simulation of individual electrons and the continuous modeling of electric fields and charging is simple: The Monte-Carlo simulation simulates a certain number of primary electrons, and then the field solver updates the field and redistributes the charge as needed. This procedure is repeated many times, typically at least once per simulated pixel. Updating multiple times for a single pixel is not unreasonable either, say after every 200 primary electrons. The detail-level interaction between the field solver, the Monte-Carlo simulation, and the charge redistribution models is more complicated. The numerical discontinuities of the electric field solution must be handled by the Monte-Carlo simulation, and the charge redistribution models tend to make the solution of the field equation more difficult and time consuming.

3.1 Electric field solver

The electric field solver uses the Poisson equation:

$$-\nabla \cdot [\epsilon_r(r) \nabla V(r)] = \frac{\rho(r)}{\epsilon_0} \quad (2)$$

in which $\rho(r)$ is the charge distribution, $V(r)$ is the potential, $\epsilon_r(r)$ is the dielectric constant of the material, and ϵ_0 is the permittivity in vacuum. To include charge redistribution effects, a space and time dependent conductivity $\sigma(r, t)$ is used with the constitutive material equation (Eq.3)

$$J = -\sigma \nabla V \quad (3)$$

and the continuity equation (Eq.4)

$$\frac{\partial \rho}{\partial t} + \nabla \cdot J = 0 \quad (4)$$

This equation (Eq. 4) is solved by an implicit Euler scheme:

$$\frac{\rho_n - \rho_{n-1}}{\Delta t} = \nabla \cdot (\sigma V_n) \quad (5)$$

where V_n is determined by

$$\frac{\rho_n}{\epsilon_0} = -\nabla \cdot (\epsilon_r \nabla V_n) = \frac{\rho_{n-1}}{\epsilon_0} + \frac{\Delta t}{\epsilon_0} \nabla \cdot (\sigma \nabla V_n) \quad (6)$$

giving a Poisson equation with modified material parameters:

$$-\nabla \cdot \left[\left(\epsilon_r(r) + \frac{\Delta t}{\epsilon_0} \sigma(r, t) \right) \nabla V_n \right] = \frac{\rho_{n-1}}{\epsilon_0} \quad (7)$$

The charges deposited during the time step by the Monte-Carlo simulation are added to ρ_{n-1} before this equation (Eq.6) is solved, which works if we just make a single time step between Monte-Carlo simulations.

The modified equation is harder to solve than the original equation, since $\sigma(r, t)$ normally changes quickly in both space and time. We previously had the option to use a direct solver as a slow but robust and accurate *reference solver*. This is no longer possible, since the expensive initial factorization must be repeated for each time step. And the geometric multigrid solver becomes less robust, because the material parameters are changing quickly on a very small spatial scale. To improve robustness, one could apply Krylov methods (i.e. preconditioned conjugate gradient, where the multigrid solver acts as preconditioner) both in the global iteration and in the W-cycle, i.e. using the K-cycle introduced by Notay et al. [37] for algebraic multigrid methods (AMG). Here W-cycle describes the process of using a multigrid solver (with just 2 iterations) to solve the problem on the coarser grid (and doing so recursively), and K-cycle describes the process of using Krylov methods (preconditioned with multigrid solver) with 2 (or very few) iterations to solve the problem on the coarser grid (and doing so recursively). But since a new reference solver is needed anyway, we started by integrating a modern algebraic multigrid solver as a first step, namely Daniel A. Spielman's modified implementation of Kyng et al. [38]. It is currently more than a factor 3 slower than the existing multigrid solver and uses significantly more memory, but it is an accurate reference solver and will also enable more flexible meshing in the near future.

3.2 Tracing electrons

The electrons both in the sample and in vacuum are traced subject to the influence of the current electric field. The numerically solved electric field is discontinuous at cell boundaries, since the finite element method (FEM) is used for discretization of the field equations. At material interfaces, the normal component of the electric field is discontinuous even for the exact solution. This severely limits the choice of reasonable integration methods. The Velocity Verlet scheme is used, because it leads to (piecewise) parabolic trajectories, for which it is easy to exactly compute the intersections with the mesh of the field solver (or the geometry). The Velocity Verlet scheme approximates the equation

$$\ddot{x}(t) = a(x(t)) \quad (8)$$

as

$$x(t + \Delta t) = x(t) + v(t)\Delta t + \frac{1}{2}a\Delta t^2 \quad (9)$$

$$v(t + \Delta t) = v(t) + \frac{a(t) + a(t + \Delta t)}{2} \Delta t \quad (10)$$

This scheme is applied with respect to time, but the simulation needs the trajectory for a given distance. If the time step Δt resulted from an intersection of the parabolic trajectory with an interface, then the corresponding distance can be computed easily with the required accuracy. If not, then Δt is determined from a given distance Δs via $\Delta t = \frac{\Delta s}{|v|}$. From a numerical point of view, this destroys the quadratic convergence order of the method. But in practice, either the electron is inside a material and Δs is very small, or the electron is in vacuum and Δs is big but irrelevant.

3.3 Modeling of sample charging

The basis for sample charging is that the creation of a secondary electron deposits a positive charge, and stopping an electron deposits a negative charge. At room temperature, both positive holes and negative electrons would continue to move and also drift in local electric fields, but modeling the movements of individual holes and electrons with thermal energy is not practical. We implemented macroscopic models for induced conductivity, dielectric breakdown, and charge diffusion. We will ignore the charge diffusion model, since we did not use it for the simulations presented later, and don't have sufficient intuition of how to set its model parameters. The motivation, modeling and implementation of the other two models are described in the following sections.

3.4 Induced conductivity

Slow electrons returning from the vacuum back to the sample tend to accumulate very close to the sample surface. The surface then tends to charge negatively and develop a dipole layer, at least in the simulation. It is not clear whether there are physical effects which could neutralize that dipole layer completely within a short time. One main charge redistribution effect is that the beam generates free holes and electrons, which locally turn insulators into conductors. This also counters that dipole layer formation, so it would be nice if this charge redistribution effect could be included in the simulation.

To avoid the complicated physics of electron and hole transport, recombination and trapping, as a first step, an established empirical quasi-static EB-induced conductivity model is attractive. The implemented model expresses the conductivity using the deposited energy per time $D(r, t)$ as

$$\sigma(r, t) = k \cdot D(r, t)^\Delta \quad (11)$$

where we used $k = 10^{-14} \text{S/m(Gy/s)}^\Delta$ (EBIC constant) and $\Delta = 1.0$ (EBIC exponent) for SiO_2 in the simulation. This model assumes a slowly changing (quasi static) deposited energy per time. However, we use it (incorrectly) for the quick scanning and a finely resolved grid with very few electrons. Still, it allows studying the impact of this sort of charge redistribution effect, and how it reduces the undesired dipole layer near the sample surface. In Kotera et al. [21], this model is used correctly for a defocused (quasi static) beam with $k = 7.7 \times 10^{-18} \text{s}^\Delta / (\Omega \cdot \text{cm} \cdot \text{rad}^\Delta)$ and $\Delta = 0.89$ for a red PMMA as given by Tanaka et al. [39]. To convert this to SI units, one has to multiply by $100 \cdot 100^\Delta$, giving $k = 4.6 \cdot 10^{-14} \text{S/m(Gy/s)}^\Delta$.

3.5 Dielectric breakdown

Even with an empirical EB-induced conductivity model as described in the previous section, one can still sometimes observe unphysically huge electric field strengths. So it makes sense to include a dielectric breakdown model as fallback for those cases where the electric field strength grows huge. That can be caused by simulation artifacts like a missing physical effect, or it can be a real physical effect, for example if two conductors are separated by a very thin insulator layer.

Instead of modeling the detailed generation of electron-hole pairs in an avalanche breakdown event, it is assumed that an isolated material will become perfectly conducting locally at the places where the field strength exceeds the dielectric strength of the material. During a breakdown event, the region where an insulator becomes conducting can travel (or grow) through space, as long as the underlying charge distribution is not sufficiently neutralized.

The model is implemented by setting the cells where the field strength currently exceeds a given threshold to perfectly conducting. Next, the field is computed again, the charges are redistributed accordingly, and then further perfectly conducting cells are added where the new field exceeds the threshold. This procedure is repeated until either the field no longer exceeds the threshold anywhere, or after the procedure was repeated a predefined number of times. The perfectly conducting region grows during the simulation of the breakdown event, but after it is finished, the previous material properties are used again, as if the breakdown would not have harmed the insulator at all. Hence it makes sense to remember any cell which temporarily got affected by breakdown (and the maximal field strength by which it got affected) for later inspection.

Having a robust breakdown model as described above is convenient, since many simulations which would otherwise have failed completely, and still yield reasonable results which can be analysed for further understanding. It is unclear to which extent other simulators also rely on that convenience. Grella et al [40] write: "Breakdown effects are taken into account by limiting the field in the sample." and Shadman et al. [41] say about the same simulator: "Still, the amount of

charge that these currents deposit can potentially raise the electric field in a dielectric to induce a current. Makeshift conductivity models have been implemented to address the resulting redistribution of the embedded charge.” Even the Java source code of JMONSEL includes a breakdown model, which was the initial motivation to investigate this sort of model.

4. RESULTS

4.1 Effect of new scattering models – no-charge up scenarios

In Figure 2, the scattering clouds of the electrons were shown. The different form of the clouds will not only make a difference on the charge distribution profile in the material, but also on the emission, especially for topographic structures. Therefore, we first test the effect of improvements independent of charging models on a topographic surface.

We simulated 200 nm pitch patterns from RM 8820 samples which have been introduced by NIST as a test and calibration standard for scanning probe microscopy [42], [43]. Amorphous silicon lines are deposited on top of a silicon substrate. In Figure 7, the cross-section view of the simulated lines is given.

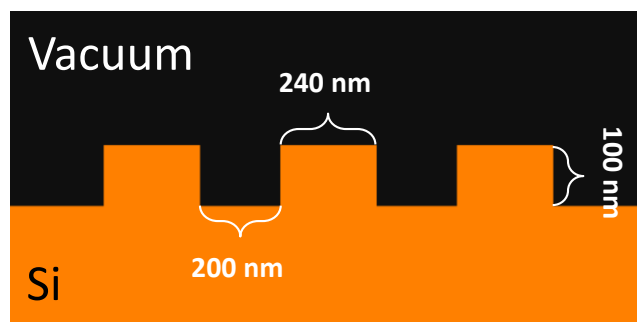


Figure 7 – The cross-section view of RM 8820 samples used to simulate. Line width is 240 nm and the height is 100 nm. The spacing is 200 nm.

The experimental results are obtained from a publication [44]. Figure 8 shows a comparison of an experimental line scan with line scans simulated using the phenomenological models from the previous study and using the first principle models introduced in this study. It is assumed that the detection efficiency is best at the top of the silicon line. Hence, the signals were aligned such that the intensities there coincide. The agreement between the experiment and the first principle model simulation used in this study is clearly better than the simulation of the previous study.

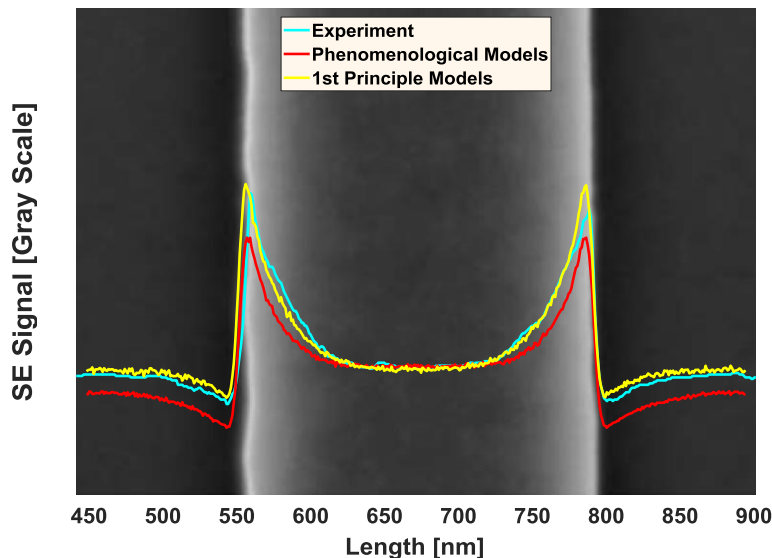


Figure 8 – SE signal from a Silicon line on top of a Silicon surface.

4.2 Effect of model improvements on SE emission

In theory, when the primary energy is in between the crossover energies E_1 and E_2 as shown in Figure 9, the total electron emission from the sample surface is more than the incident primary current ($I/I_p > 1$). Therefore, it is expected that a dielectric material gets positively charged. However, it is reported [7] that the positive charge-up process is self-regulatory due to recollection of the electrons by the sample. Therefore, the total yield (SE + BSE) becomes ~ 1 .

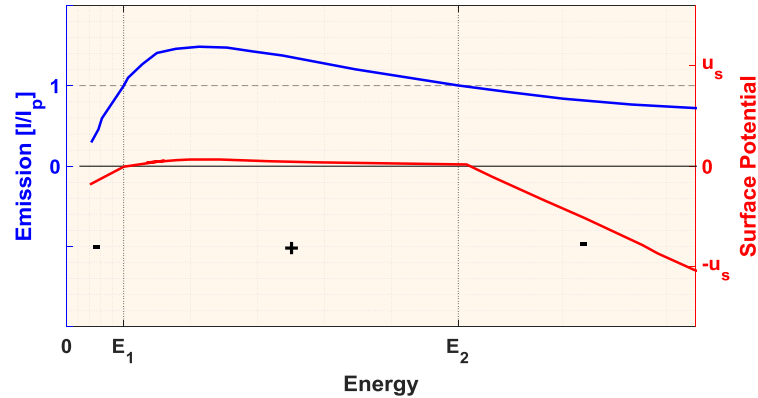


Figure 9 – Surface potential of insulators during charging process.

The “nominal” SE yield from SiO_2 is ~ 7 at 1 keV. We call it nominal because no charge-up is allowed. In a more realistic scenario, when scanning the primary beam across the sample, the expectation is that the SE-yield drops along the scan line due to the positive surface potential, i.e. a drop in the signal is observed. Therefore, we test the simulator to observe the described phenomenon.

The first two steps of a line scan on bulk material are shown in Figure 10. The scan area is $100 \mu\text{m}$ and the pixel size is 2.5 nm . The beam energy and size are 1 keV and 3 nm (FWHM), respectively. The dose is $250 \mu\text{C}/\text{cm}^2$ (100 electrons per pixel) and the electric field is updated for every pixel with the AMG solver. The beam current is 100 pA . Breakdown module is enabled with threshold value of $50 \text{ MV}/\text{m}$.

Until the first computation of the electric field, the SiO_2 sample stays neutral and all of the emitted electrons reach the detector above the sample (in Figure 10, left). After the field is computed from the charge distribution obtained from the previous scattering events (left inset Figure 10), electrons start to experience the positive potential at the surface and the electrons with energy less than the surface potential return to the sample (Figure 10, right, the inset shows the field and the returning electron trajectories). It is observed that the (maximum) potential increases (0 V , 3.726 V , 4.688 V ...) for the first couple of pixels and then saturates around $\sim 10 \text{ V}$. The effect of the charging on the emission is shown in Figure 11a. As expected the total emission is high for a couple of pixels, then decreases and it saturates after $\sim 25 \text{ nm}$ (10 pixels). The stable BSE emission indicates that the surface potential stays rather small which only affects the low energetic SEs.

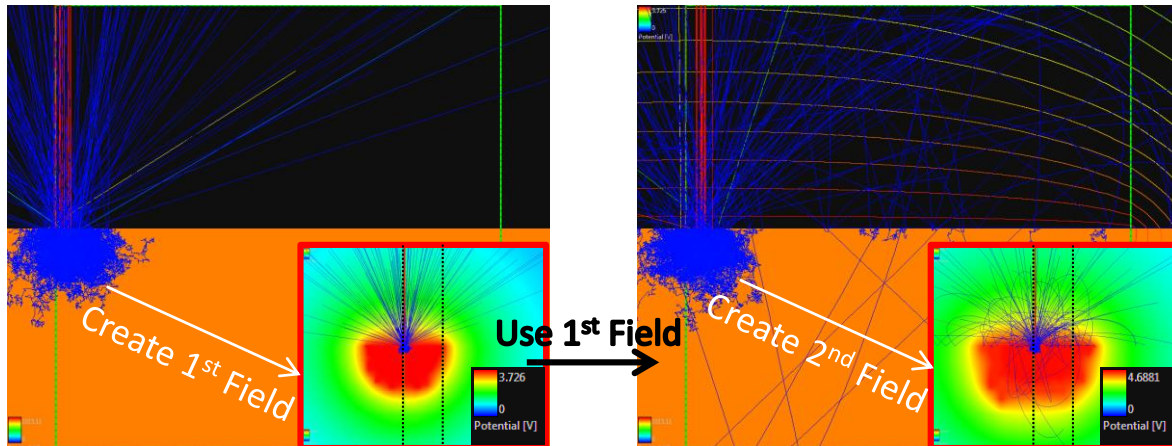


Figure 10 – Charging simulation of a line scan: the initial two steps are depicted. In the beginning (left-big view), there is no field. Hence, the trajectories (red for high energy; blue for low energy electrons) are straight. After the scattering is completed, the electric field is calculated with the distributed charges in the material (the inset in the left figure, note that the scale is different from the big view image). The simulator uses the computed e-field to trace the electrons of the next beam position. Iso-lines indicate the presence of fields in the right figure (big-view). Similarly, the electric field is computed for the next beam in the linescan. As the SEs are recollimated by the positive surface potential (the inset in the right figure), the signal drops.

When the charging dose is decreased to $25 \mu\text{C}/\text{cm}^2$ (10 electrons per pixel) to, the number of created charge carriers per voxel is less. Therefore, the magnitude of the local field becomes smaller than at higher dose and more electrons can reach the detector. In Figure 11b, the corresponding signal drop saturates after about 100 nm which causes a larger bright-to-dark transition area on the SEM image. The increased noise in the signal is due to shotnoise, being larger for a lower amount of electrons in the probe.

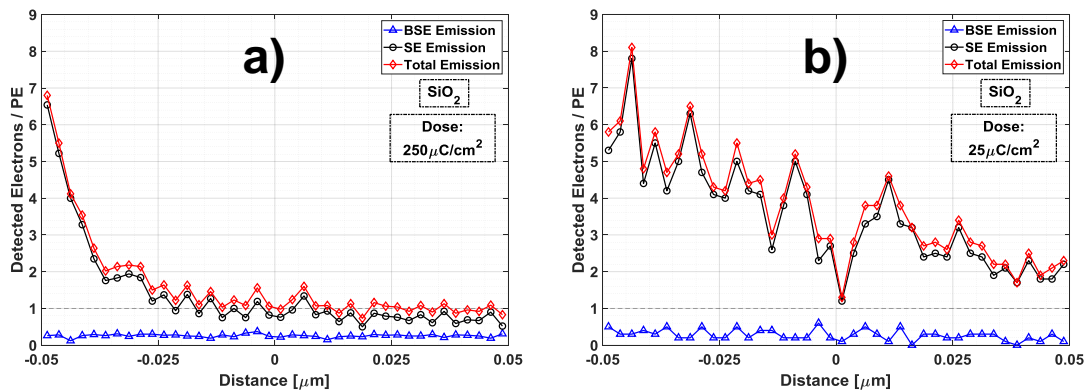


Figure 11 – The effect of dose on emission: when dose is a) $250 \mu\text{C}/\text{cm}^2$; b) $25 \mu\text{C}/\text{cm}^2$.

The results show that the simulations are sensitive to parameters affecting the charge carrier density, such as the dose. This can lead different to results in measurements with dielectrics where contrast is playing a role.

4.3 Effect of model improvements on the grating coupler simulations

In the previous study, the grating coupler is described in detail. In Figure 12 (left), a top-down view of the device is shown. The middle figure shows a zoomed-in image of the 2nd trench, and the right-hand figure shows the intensity profile across that trench. Note that, the scan direction is from left-to-right (fast-scan axis) and top-to-bottom (slow-scan axis). The topographic contrast is visible on the surrounding silicon structures and also on the oxide inside of the trenches. In addition, there is an extra contrast in the trenches along the fast-scan direction, which is asymmetric in the intensity profile. That is, the peak intensity along the x-axis is positioned left from the center of the trench. This can be explained as follows. The electron probe visits the left side of the oxide in the trench first and creates a positive surface

potential. As it visits the next pixels of the scanline, the surface potential slightly accumulates and causes a drop of the signal for those pixels. The phenomenon qualitatively agrees with the theory described in section 4.2.

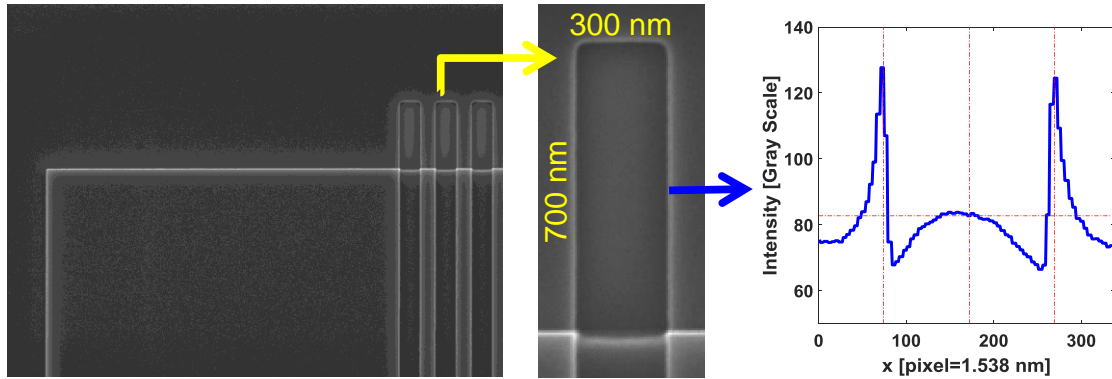


Figure 12 – Experiment: top-down view of the vertical lines. Left: grating coupler experiment at 4 keV; Middle: zoomed-in view to the 2nd trench; Right: integrated signal profile (10 pixel in y-axis) of the middle image.

When simulating these trenches, including charging, a similar effect (bright-to-dark contrast) is observed (see Figure 13). It does not yet show all the features shown in Figure 12, but it does show the asymmetry in the contrast across the trench, which could not be achieved in our previous work. In this simulation, the region of interest is about $\sim 1.5 \mu\text{m}^2$ ($1.1 \mu\text{m} \times 1.5 \mu\text{m}$). The pixel size is 5 nm and the charging dose is $25 \mu\text{C}/\text{cm}^2$ (40 electrons per pixel). The simulation without charging took 4 hours 13 minutes on a typical quad-core laptop. The simulation with charging took 13 hours and 50 minutes on a 64-core workstation, with Monte-Carlo parallelization, but without parallelization of the field solver.

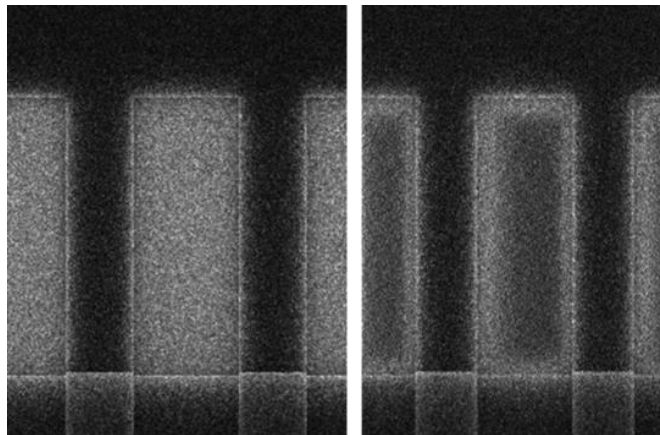


Figure 13 - Simulated trenches of the grating couplers. Left: image simulated without charging models; Right: image simulated with charging models.

4.4 The Effect of the EBIC model

We show the impact of the charge redistribution model on Cu pads embedded in a thin SiO_2 layer on top of a Si wafer. The pads 1, 2 and 4 are electrically floating (no contact to the underlying Si wafer), and pad number 3 is connected to the underlying Si wafer (Figure 14).

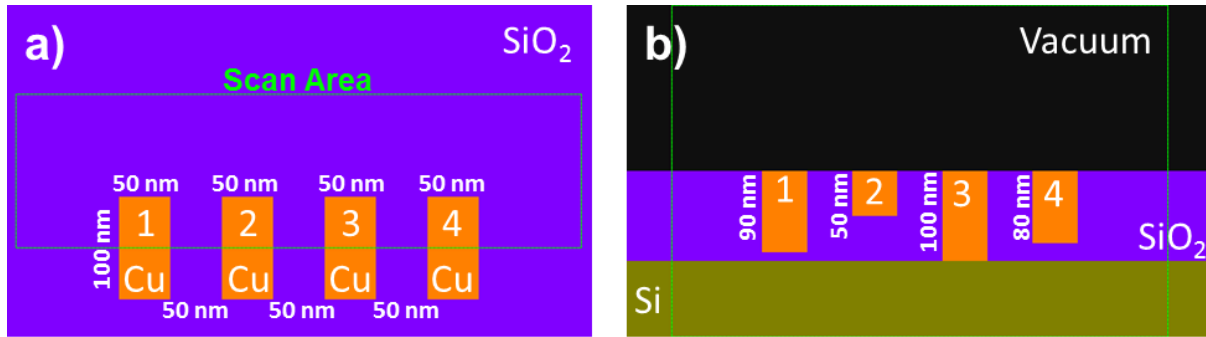


Figure 14 - Sketch of the geometry of the 4 copper pads: a) a top-down and b) a cross-section view. The green lines correspond to the imaging area.

In Figure 15, the effect on the simulated SEM images is shown when the charging model and/or EBIC model is switched on. When the charging model, and the EBIC model too, is switched-off, copper contacts appears darker due to its lower SE yield relative to SiO_2 at 0.75 keV in Figure 15b. Furthermore, the conductive pad (3) is indistinguishable from the others. When the charging model is switched on, but the EBIC model is off, the emission of the oxide gets lower due to the positive surface potential and the SE yield becomes comparable to the copper contacts (Figure 15c). Note that the conductive pad appears different than the other pads because conductivity allows it to conduct charge carriers to ground. The EBIC model leads to more realistic images of the contact pads and the surrounding insulating areas. When the EBIC model is switched-on, the oxide surrounding region of the conductive pad experiences induced conductivity and charge carriers are conducted to ground and no charging occurs. As a result, the oxide shows the nominal SE yield and becomes brighter than other features.

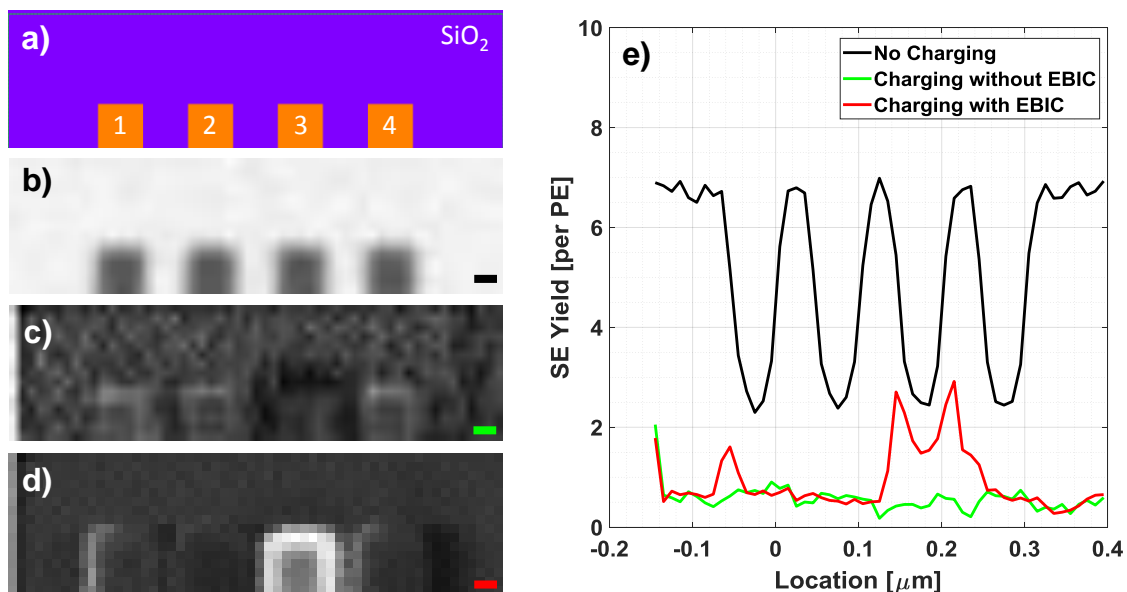


Figure 15 - SEM image simulation of the copper pads, a), in Figure 14 when b) charging and EBIC are switched-off; c) charging is switched-on but EBIC model is off; d) both charging and EBIC models are switched on. Scale bars are 100 nm. The intensity profiles at d) are obtained from the level of the scale bars (25 nm) along the images. At 0.75 keV, positive charges on the surface retract secondary electrons and the signal intensity decreases. However, the electrically connected copper pad stays neutral and the surrounding area of the pad shows conduction due to EBIC and signal drop does not occur fully due to positive charging.

5. CONCLUSIONS

Model improvements for Monte-Carlo simulations were presented. These improvements include both low energy electron scattering and charging-up of dielectrics. First of all, we have included first principle scattering models to simulate electron-matter interactions in order to more precisely predict charge distributions in the material. The latter involves models which couple dynamically with the charge distribution, such as calculation of local fields, tracing of the electrons in the field and redistribution of the charges in the materials. For instance, the redistribution models, EBIC and dielectric breakdown, help to include induced conductivity in dielectric materials.

Firstly, we have shown that including first principle scattering models, especially electron-phonon scattering, leads to a more realistic charge distribution inside the material. Although the generation and tracing of every electron in the field increases the computation time significantly, we tried to avoid simplifications/optimization of the scattering models.

In an earlier study, the charge mobility was not allowed in the dielectrics. This was causing accumulation of unrealistically big potentials, causing beam deflections. Introducing redistribution of the charges helped to solve these artifacts. The models incorporate tracing of all the electrons with a higher accuracy in the electric field, enabling us to reproduce contrast changes due to the surface potential. This results in better yields and more realistic energy analysis of the emitted electrons.

In addition, the EBIC model allowed simulation of induced conductivity effects where the presence of the beam increases the conductivity of the dielectric material, creating a conductive channel to neighboring conductive materials at ground potential.

Future steps will include parallelization of the field solver, to speed up the simulations. Improvements in the modelling can be considered by including surface plasmons and trapping. More accurate material parameters will also increase accuracy.

ACKNOWLEDGMENTS

We would like to thank Jens Bolten for his assistance and for providing experimental results. KTA would like to express his sincere thanks to Thomas Verduin, Annemarie Theulings and Luc van Kessel for fruitful discussions on the physics of the electron-matter interactions. TK is grateful to John Villarrubia for providing the source code of JMONSEL, which provoked the idea of the dielectric breakdown model.

REFERENCES

- [1] Kotera, M., and Suga, H., "A simulation of keV electron scatterings in a charged-up specimen," *J. Appl. Phys.*, 63, 261, (1988).
- [2] Seeger, A., Duci, A. and Haussecker, H., "Scanning electron microscope charging effect model for chromium/quartz photolithography masks," *Scanning.*, 28, 179, (2006).
- [3] Postek, M.T. and Vladár, A.E. "Does your SEM really tell the truth? How would you know? Part 4: Charging and its Mitigation," *Proc. SPIE 9636*, 963605, (2015).
- [4] Ichinokawa, T., Iiyama, M., Onoguchi, A. and Kobayashi, T., "Charging effect of specimen in scanning electron microscopy," *Jpn. J. Appl. Phys.*, 13, 1272, (1974).
- [5] Okai, N. and Sohda, Y., "Study on image drift induced by charging during observation by scanning electron microscope," *Jpn. J. Appl. Phys.*, 51, (2012).
- [6] Cazaux, J., "On some contrast reversals in SEM: Application to metal/insulator systems," *Ultramicroscopy*, 108, 1652, (2008).
- [7] Reimer, L., [Scanning Electron Microscopy], Springer, 2nd ed., (1998).
- [8] Orloff, J., [Handbook of Charged Particle Optics], CRC Press, 2nd ed., (2009).
- [9] Davidson, M.P., Sullivan, N.T., Company, S., Ave, S.L. and View, M., "An Investigation of the Effects of Charging in SEM based CD Metrology," *SPIE*. 3050, 226, (1997).
- [10] Abe, H., Babin, S., Borisov, S., Hamaguchi, A., Kadowaki, M. and Yamazaki, Y., "Contrast reversal effect in scanning electron microscopy due to charging," *J. Vac. Sci. Technol. B.*, 27, 1039, (2009).

- [11] Li, Y.G., Zhang, P. and Ding, Z.J., "Monte Carlo Simulation of CD-SEM Images for Linewidth and Critical Dimension Metrology," *Scanning*, 35, 127, (2013).
- [12] Ganachaud, J.P. and Mokrani, A., "Theoretical study of the secondary electron emission of insulating targets," *Surf. Sci.*, 334, 329, (1995).
- [13] Fitting, H.J. and Touzin, M., "Secondary electron emission and self-consistent charge transport in semi-insulating samples," *J. Appl. Phys.*, 110, (2011).
- [14] Cao, M., Wang, F., Liu, J. and Zhang, H.B., "Charging dynamics of a polymer due to electron irradiation: A simultaneous scattering-transport model and preliminary results," *Chinese Phys. B.*, 21 (2012).
- [15] Grella, L., Lorusso, G., Lee, P., Frank, F. and Adler, D.L., "Three-dimensional simulation of top down scanning electron microscopy images," *J. Vac. Sci. Technol. B.*, 22, 3399, (2004).
- [16] Babin, S., Borisov, S., Ivanchikov, A. and Ruzavin, I., "CHARIOT: Software tool for modeling SEM signal and e-beam lithography," *Phys. Procedia.*, 1, 305, (2008).
- [17] Ohya, K. and Kuwada, H., "Modeling of Electron Beam Charging of an Insulating Layer on a Silicon Substrate," *E-Journal Surf. Sci. Nanotechnology*, 9, 112, (2011).
- [18] Ilgüsatiroglu, E., Illarionov, A.Y., Ciappa, M., Pfäffli, P. and Bomholt, L., "New integrated Monte Carlo code for the simulation of high-resolution scanning electron microscopy images for metrology in microlithography," *Proc. SPIE.*, 9050, (2014).
- [19] Villarrubia, J.S., Vladár, A.E., Ming, B., Kline, R.J., Sunday, D.F., Chawla, J.S. and List, S., "Scanning electron microscope measurement of width and shape of 10nm patterned lines using a JMONSEL-modeled library," *Ultramicroscopy*, 154, 15, (2015).
- [20] Arat, K.T., Bolten, J., Klimpel, T. and Unal, N., "Electric fields in Scanning Electron Microscopy simulations," *Proc. SPIE.*, 9778, (2016).
- [21] Kotera, M., Yamaguchi, K. and Suga, H., "Dynamic Simulation of Electron-Beam-Induced Chargingup of Insulators," *Japanese J. Appl. Physics*, 38, 7176, (1999).
- [22] Salvat, F., Jablonski, A., Powell, C.J., "ELSEPA—Dirac partial-wave calculation of elastic scattering of electrons and positrons by atoms, positive ions and molecules," *Comput. Phys. Commun.*, 165, 157, (2005).
- [23] Kieft, E. and Bosch, E., "Refinement of Monte Carlo simulations of electron–specimen interaction in low-voltage SEM," *J. Phys. D. Appl. Phys.*, 41, (2008).
- [24] Verduin, T., [Quantum Noise Effects in e-Beam Lithography and Metrology], Delft University of Technology, (2016).
- [25] Winter, M., "WebElements." [Online]. Available: <http://www.webelements.com>. (Accessed: 23-Jan-2018).
- [26] Theodore, M.N., Max, W., "Periodictable.com," [Online]. Available: <http://periodictable.com/Elements/029/index.html>. (Accessed: 23-Jan-2018).
- [27] Haynes, W.M., [CRC handbook of chemistry and physics: a ready-reference book of chemical and physical data], CRC Press, FL., (2011).
- [28] Kasap, S.O., [Principles of electronic materials and devices], McGraw-Hill, Boston, (2001).
- [29] Kuhr, J.C. and Fitting, H.J., "Monte-Carlo Simulation of Low Energy Electron Scattering in Solids," *Phys. Status Solidi.*, 172, 433, (1999).
- [30] Van Zeghbroeck, B. J., "Effective mass in semiconductors", *Princ. Semicond. Devices*, (1997). Available: <https://ecee.colorado.edu/~bart/book/effmass.htm>.
- [31] Schreiber, E., and Fitting, H.J., "Monte Carlo simulation of secondary electron emission from the insulator SiO₂," *J. Electron Spectros. Relat. Phenomena.*, 124, 25, 2002).
- [32] Madelung, O., Rössler, U. and Schulz, M., "Silicon (Si), sound velocities: Datasheet from Landolt-Börnstein - Group III Condensed Matter · Volume 41A1β: "Group IV Elements, IV-IV and III-V Compounds. Part b - Electronic, Transport, Optical and Other Properties," SpringerMaterials.
- [33] Madelung, O., Rössler, U. and Schulz, M., "Silicon (Si), deformation potentials: Datasheet from Landolt-Börnstein - Group III Condensed Matter · Volume 41A1β: "Group IV Elements, IV-IV and III-V Compounds. Part b - Electronic, Transport, Optical and Other Properties" SpringerMaterials.
- [34] Joy, D. and Luo, S., "An empirical stopping power relationship for low energy electrons," *Scanning*, 11, 176, (1989).
- [35] Ashley, J.C., "Interaction of low-energy electrons with condensed matter: stopping powers and inelastic mean free paths from optical data," *J. Electron Spectros. Relat. Phenomena.*, 46, 199, (1988).
- [36] Kaneko, T., "Energy distribution of secondary under electron bombardment electrons emitted from solid surfaces," *Surf. Sci.*, 237, 327, (1990).

- [37] Notay, Y. and Panayot, V., "Recursive Krylov-based multigrid cycles" *Numer. LINEAR Algebr. WITH Appl.*, 16, 473, (2007).
- [38] Kyng, R. and Sachdeva, S., "Approximate Gaussian Elimination for Laplacians - Fast, Sparse, and Simple," *Proc. - Annu. IEEE Symp. Found. Comput. Sci., FOCS. 2016–Decem*, 573, (2016).
- [39] Tanaka, R., Hiromi, S. and Tamura, N., "The Effect of Accumulated Charge on Depth Dose Profile in Poly(Methylmethacrylate) Irradiated with Fast Electron Beam," *IEEE Trans. Nucl. Sci., NS-26*, 4670, (1979).
- [40] Luca, G., Lorusso, G. and Adler, D.L., "Simulations of Scanning Electron Microscopy Imaging and Charging of Insulating Structures," *Scanning*, 25, 300, (2003).
- [41] Shadman, K and De, I., "Analytic models for the kinetics of generating a voltage contrast signal from contact plugs used in integrated circuits Analytic models for the kinetics of generating a voltage contrast signal," (2007).
- [42] Postek, M.T. and Watters, R.L., "Report of Investigation: Reference Material 8820 Scanning Electron Microscope Scale Calibration Artifact Reference," *Reference*, 1, (2009).
- [43] Postek, M.T., Vladar, A.E. and Keery, W., "Reference material (RM) 8820: A versatile new NIST standard for nanometrology," *Proc SPIE.*, 7638, (2010).
- [44] Postek, M.T., Villarrubia, J.S. and Muto, A., "Comparison of Electron Imaging Modes for Dimensional Measurements in the Scanning Electron," 1, (2016).